DOI: 10.1111/cgf.14293
Eurographics Conference on Visualization (EuroVis) 2021
R. Borgo, G. E. Marai, and T. von Landesberger
(Guest Editors)

Volume 40 (2021), Number 3

Local Extraction of 3D Time-Dependent Vector Field Topology

Lutz Hofmann and Filip Sadlo

Heidelberg University, Germany

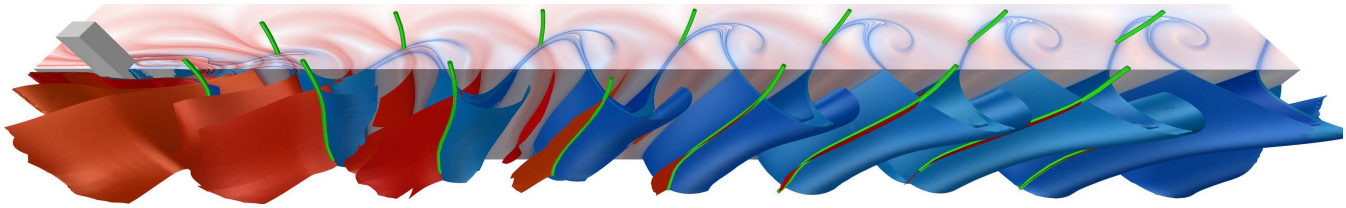

Figure 1: *Time-dependent vector field topology of the von Kármán Vortex Street dataset at t=0.5 s, defined by attracting/repelling Lagrangian coherent structures (LCS, blue/red surfaces), obtained as streak manifolds seeded along hyperbolic path surfaces (time slice by green lines). Our local extraction yields a geometric representation of the temporal evolution of the LCS, which is consistent with ridges in the backward- (blue) and forward-time (red) FTLE fields. Sections of the FTLE fields shown in the back half, streak manifolds clipped at the top for clarity.*

Abstract

We present an approach to local extraction of 3D time-dependent vector field topology. In this concept, Lagrangian coherent structures, which represent the separating manifolds in time-dependent transport, correspond to generalized streak manifolds seeded along hyperbolic path surfaces (HPSs). Instead of expensive and numerically challenging direct computation of the HPSs by intersection of ridges in the forward and backward finite-time Lyapunov exponent (FTLE) fields, our approach employs local extraction of respective candidates in the four-dimensional space-time domain. These candidates are subsequently refined toward the hyperbolic path surfaces, which provides unsteady equivalents of saddle-type critical points, periodic orbits, and bifurcation lines from steady, traditional vector field topology. In contrast to FTLE-based methods, we obtain an explicit geometric representation of the topological skeleton of the flow, which for steady flows coincides with the hyperbolic invariant manifolds of vector field topology. We evaluate our approach on analytical flows, as well as data from computational fluid dynamics, using the FTLE as a ground truth superset, i.e., we also show that FTLE ridges exhibit several types of false positives.

CCS Concepts

• ***Human-centered computing*** → ***Visualization techniques;*** • ***Applied computing*** → *Mathematics and statistics;*

1. Introduction

During the last three decades, vector field topology has become a well established and very successful approach for visualizing vector fields. By separating their regions with qualitatively different behavior, it provides a representation of their overall transport structure. The traditional vector field topology [HH91] (VFT) applies to steady, i.e., time-independent vector fields, and separates the regions by means of so-called separatrices. The separatrices are obtained from saddle-type critical points (isolated zeros) and saddle-type periodic orbits (isolated closed streamlines), where the saddle property, also denoted hyperbolic, means that there is at least one manifold of streamlines converging to the structure in forward time, and at least one manifold converging to it in reverse time. These manifolds are the separatrices, and they consist of streamlines integrated for infinite time in forward and reverse direction. Although non-separating structures, such critical points / periodic orbits of type sink (all streamlines converging in forward time) and source (all streamlines converging in reverse time) as well as invariant tori, are often additionally included in the topological skeleton, they do not give rise to separatrices. Since, in addition, in time-dependent vector fields counterparts to separatrices are widely present as Lagrangian coherent structures, but counterparts to sources and sinks exist only in special configurations, time-dependent vector field topology is primarily concerned with the separating structures. On the other hand, only comparably recently it has been acknowledged that boundary switch curves [WTHS04] and bifurcation lines [PC87, Rot00, MSE13] along with their separatrices need to be included in the topological skeleton to obtain

all separating structures in VFT. Streamlines seeded along boundary switch curves provide separatrices that separate "interior flow" from flow that passes domain boundaries, whereas bifurcation lines consist of "longest flow-aligned" sets of points of saddle-type flow behavior that give rise to separatrices as well (see Figure 8a). The steady VFT defined by saddle-type critical points together with periodic orbits, bifurcation lines, as well as attachment and separation lines, in a suitable frame of reference, provides candidate structures for our extraction of the time-dependent 3D vector field topology.

Due to its instantaneous nature, VFT cannot reflect the true transport in time-dependent flow. Furthermore, its strictly infinite-time concept would often not even be applicable, since aperiodic time-dependent fields are typically defined on finite time domains. Providing a solution to both of these shortcomings, the finite-time Lyapunov exponent (FTLE) has become a successful technique for direct visualization of the finite-time separation of particles [Hal01]. Some ridges in the FTLE field represent Lagrangian coherent structures [SLM05] (LCS), the time-dependent counterpart to separatrices. A shortcoming with this approach is, however, that not all FTLE ridges represent LCS, i.e., a substantial number of the ridges can be induced by shear flow and is thus not separating. The LCS, i.e., the separating ones, are also denoted hyperbolic FTLE ridges. If one computes the FTLE field for steady vector fields, saddle-type critical points coincide with intersections of forward and reverse hyperbolic FTLE ridges, also called hyperbolic trajectories (HT). That is, the concepts are consistent. In time-dependent flow, however, intersections of hyperbolic FTLE ridges do not necessarily represent HTs, since such intersections can also be caused by FTLE ridges emanating from remote hyperbolic trajectories [HS20]. Further drawbacks with FTLE-based visualization include that the FTLE field requires computationally costly integration of pathlines seeded on a dense grid in space and time, and that the extraction of ridges therefrom is numerically challenging [GGTH07, SP07].

An approach complementary to the FTLE obtains the LCS by generating manifolds of streaklines, seeded along the HTs [SW10, USE13, MBES16, HS20]. It has the advantage that the LCS are obtained at much higher accuracy, since the streak manifolds are attracted to the respective LCS during integration, and at much lower computational cost, because only the streak manifolds of the LCS have to be integrated, instead of computing the dense grid of pathlines in the entire domain to obtain the FTLE field. The first approaches for streak-based topology extracted the HTs by computing the forward and reverse FTLE fields, extracting their ridges, and intersecting them. The FTLE fields were either computed only sparsely in time [SW10, USE13], which required integration of the HTs from the intersections and involved exponential error growth due to the repelling property of LCS in either time direction, or the FTLE computation was dense in space and time [BSDW12], which led to very high computational cost. Notice that the width of FTLE ridges tends to decrease exponentially with increasing integration time, and thus very high spatial resolutions are required to avoid aliasing [SJS20]. For 2D time-dependent vector fields, more recent approaches obtain the HTs without the help of the FTLE, by extracting them as bifurcation lines in the 3D ("stacked") space-time representation of the time-dependent field [MBES16], with the most recent contribution [HS20] providing robust and highly accurate extraction of the HTs and the resulting streak manifolds.

This paper can be seen as an extension of the previous work [HS20] from 2D to 3D time-dependent vector fields. As we will show, however, such extension is far from straightforward and poses many new challenges that require different solutions. In addition, we address issues that have not yet been sufficiently addressed in the 2D case [HS20]. Specifically, our contributions include:

- Local extraction of HT surface candidates in 4D space-time,
- robust and accurate refinement of the candidates to HT surfaces,
- demonstration of the necessity to additionally include unsteady equivalents of bifurcation lines, spiral saddle critical points, a class of saddle-type periodic orbits, and saddle connectors, and
- automatic selection of seeding lengths.

2. Related Work

An overview of time-dependent vector field topology was recently presented by Bujack et al. [BYH*20]. The authors propose a set of desirable properties for time-dependent vector field topology, which we relate to our approach in Section 4.5.

Üffinger et al. [USE13] extended the 2D streak topology [SW10] described above to 3D time-dependent vector fields. Similarly to Sadlo and Weiskopf, the authors seed path surfaces at intersection curves of the ridge surfaces in the forward and reverse FTLE fields. In the 2D case, Machado et al. [MBES16] showed, that hyperbolic trajectories can be more efficiently extracted as space-time bifurcation lines, i.e., by refining parallel vectors [PR99] lines extracted from the space-time vector field. As noted by Günther et al. [GGT17], these parallel vectors lines correspond to tracked critical points in the Galilean-invariant frame of reference defined by the feature flow field [TS03]. The former authors solve linear least squares problems in a local neighborhood to obtain optimal frames of reference based on objective transformations. This approach has been extended to affine and displacement transformations [GT20, RG20]. Hadwiger et al. [HMTR18] propose a global optimization scheme, which we do not consider here due to its high computational cost. Its temporally smooth observers could, however, be used for more accurate initial candidates for refinement in our approach. Hofmann and Sadlo [HS20] refined paths of critical points in the optimal reference frames by employing a technique for computing distinguished hyperbolic trajectories, originally proposed by Ide et al. [ISW02], in order to obtain a more robust extraction of 2D time-dependent vector field topology. Branicki and Wiggins [BW09] extended the approach for extracting distinguished hyperbolic trajectories to 3D, where they employ paths of critical points in the lab frame as initial candidate lines. As shown by Üffinger et al. [USE13], this approach based on hyperbolic trajectories instead of hyperbolic path surfaces misses large parts of LCS in typical numerical datasets. In this work, we base candidate extraction on the notion of bifurcation surfaces, which have been defined in arbitrarily-dimensional flows by Hofmann and Sadlo [HS19] by means of the dependent vectors operator. Similarly to the coplanar vectors operator for unsteady vortex core lines [WSTH07], a direct application of the dependent vectors operator to the space-time vector field would result in tracked bifurcation lines in the Galilean-invariant frame of reference defined by the feature flow field. However, such direct application fails for typical numerical datasets, necessitating alternative approaches.

Separatrices in our approach are obtained as generalized streak surfaces, which, in analogy to generalized streaklines introduced by Wiebel et al. [WTS*07], are seeded along time-varying seeding curves. For their computation, we employ the algorithm by Krishnan et al. [KGJ09], which outputs a representation of the entire time-varying streak surface by recording the topological changes to the triangle mesh alongside the required pathlines. We employ a modification of their streak seeding approach based on time-varying curves, tailored to the use of space-time seeding surfaces.

3. Fundamentals

We consider a 3D time-dependent vector field $\mathbf{u}(\mathbf{x},t) \in \mathbb{R}^3$ with $\mathbf{x} \in \Omega \subseteq \mathbb{R}^3$, defined over a finite time interval $t \in [t_{\min}, t_{\max}]$. Massless particles move within this space along tangent lines $\mathbf{x}(t)$, i.e., $\mathrm{d}\mathbf{x}(t)/\mathrm{d}t = \mathbf{u}(\mathbf{x}(t),t)$ with initial value $\mathbf{x}(t_0) = \mathbf{x}_0$. The phase space of its associated dynamical system is the four-dimensional space-time domain $\Omega \times [t_{\min}, t_{\max}]$.

3.1. Hyperbolic Trajectories

In this paper, we consider the qualitative structure w.r.t. separating and attracting behavior of close-by particles. In first-order approximation, the evolution of infinitesimal perturbations $\boldsymbol{\delta}_\mathbf{x}(t)$ along a trajectory $\mathbf{x}(t)$ is described by the localized system [ISW02]

$$\frac{\mathrm{d}}{\mathrm{d}t}\boldsymbol{\delta}_\mathbf{x}(t) = \nabla\mathbf{u}(\mathbf{x}(t),t)\boldsymbol{\delta}_\mathbf{x}(t)\,. \tag{1}$$

Its fundamental solution matrix is the 3×3 matrix $\mathbf{X}(t)$ with initial condition $\mathbf{X}(t_0) = \mathbb{I}$, whose singular values $\sigma_1(\mathbf{X}(t)) \le \sigma_2(\mathbf{X}(t)) \le \sigma_3(\mathbf{X}(t))$ describe the lengths of the principal axes of the ellipsoid spanned by the columns of $\mathbf{X}(t)$, which limits all maximum perturbations at time t. Given, that the trajectory is defined over the time interval $t \in [t_0, t_N]$, we obtain the finite-time Lyapunov exponents

$$\lambda_i = \frac{1}{|t_N - t_0|}\ln\sigma_i(\mathbf{X}(t_N))\,, \quad i = 1,2,3\,. \tag{2}$$

We call a trajectory hyperbolic, if $\lambda_1 < 0 < \lambda_3$. In this case, λ_1 describes the exponential rate of contraction along the trajectory, and λ_3 describes the exponential rate of expansion. Similarly to saddle-type critical points in 3D steady vector fields, the medium Lyapunov exponent λ_2 can either be positive or negative. This trajectory-centric view is formalized by the time-dependent coordinate transform [ISW02]

$$\mathbf{T}(t) = e^{(t-t_0)\mathbf{D}}\mathbf{R}(t_N)\mathbf{X}^{-1}(t)\,, \tag{3}$$

where $\mathbf{D} = \mathrm{diag}(\lambda_1,\lambda_2,\lambda_3)$ is the diagonal matrix containing the Lyapunov exponents, and $\mathbf{R}(t_N)$ is the right factor in the singular value decomposition $\mathbf{X}(t) = \mathbf{B}(t)\mathbf{S}(t)\mathbf{R}(t)$. The localized flow is transformed by $\mathbf{y}(t) = \mathbf{T}(t)\boldsymbol{\delta}_\mathbf{x}(t)$ into the steady system

$$\frac{d}{dt}\mathbf{y}(t) = \mathbf{D}\mathbf{y}(t)\,, \tag{4}$$

where the attracting and repelling behavior is separated, and thus enables decoupled refinement of a HT. Notice that without such decoupling, there is repelling dynamics in both time directions, which impedes refinement (Section 4.2). The columns of the inverse coordinate transform $\mathbf{T}^{-1}(t)$ are the Lyapunov vectors $\boldsymbol{\xi}_i(t) = \mathbf{T}^{-1}(t)\mathbf{e}_i$, which describe the perturbation directions, that the respective Lyapunov exponents belong to. We are going to only consider hyperbolic trajectories, that are also instantaneously hyperbolic, in the sense that the Jacobian $\nabla\mathbf{u}(\mathbf{x}(t),t)$ has eigenvalues with positive and negative real parts for all t. We note, that unlike in 2D flows, this condition does not imply that the Jacobian has real eigenvalues. Existing literature [ISW02, BW09] only considers isolated, distinguished HTs, often obtained from paths of critical points. However, as we discuss next, in the 3D case it is necessary to consider *surfaces* consisting of (non-distinguished) HTs.

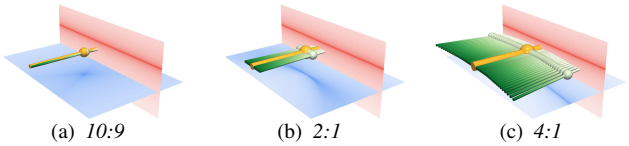

(a) *10:9* (b) *2:1* (c) *4:1*

Figure 2: *Hyperbolic trajectories (HT) for a saddle-type critical point (with different anisotropy ratios of $\lambda_1 : \lambda_2$) moving from left to right. Only almost isotropic (a) configurations exhibit isolated HTs, whereas a single HT (orange) only captures a subset of the the FTLE ridge intersection in generic anisotropic cases (b),(c). Hyperbolic path surface with time from green to white, forward (red) and backward (blue) FTLE slices shown at the time depicted by the spheres, where FTLE ridges intersect in a point ((a), ridge line and ridge surface), and in a line ((b),(c), two ridge surfaces).*

3.2. Lagrangian Coherent Structures

As an indicator for separating behavior of trajectories, the flow map $\boldsymbol{\phi}_{t_0}^T(\mathbf{x})$ is employed, which maps particles seeded at $\mathbf{x}$ at time t_0 to their positions after integration time T. Given a trajectory seeded at $\mathbf{x}(t_0) = \mathbf{x}_0$, the fundamental matrix $\mathbf{X}(t)$ of its localized flow (Equation 1) coincides with the flow map gradient $\nabla\boldsymbol{\phi}_{t_0}^{t-t_0}(\mathbf{x}_0)$. The finite-time Lyapunov exponent field $\varsigma_{t_0}^T(\mathbf{x})$ is defined as the largest Lyapunov exponent of the trajectory seeded at $\mathbf{x}$ at time t_0,

$$\varsigma_{t_0}^T(\mathbf{x}) = \frac{1}{|T|}\ln\sigma_3\Big(\nabla\boldsymbol{\phi}_{t_0}^T(\mathbf{x})\Big)\,. \tag{5}$$

Ridge surfaces [EGM*94] in the forward-time ($T > 0$) FTLE field, that represent material surfaces and are locally most repelling, coincide with repelling LCS. Analogously, a subset of the ridge surfaces in the reverse-time FTLE field $\varsigma_{t_0}^{-T}(\mathbf{x})$ coincides with attracting LCS. As introduced above, these forward- and backward-time FTLE ridges are also denoted hyperbolic.

Intersections of hyperbolic ridges in the forward- and reverse-time FTLE fields include hyperbolic trajectories. They are those trajectories, that stay in an instantaneously hyperbolic region locally for the longest time [Hal01], and can also be regarded as a finite-time approximation of distinguished hyperbolic trajectories (DHTs) [ISW02]. Note, that in 3D flows, such ridge surface intersections are in general curves (Figure 2), and thus represent surfaces in the space-time domain [USE13], not curves. This means, that due to the finite time interval, trajectories that pass through these intersection curves cannot be distinguished and all equally contribute to the organization of the flow. We call these surfaces hyperbolic path surfaces (HPS), if they do not represent intersections of our streak manifolds generated from hyperbolic path surfaces, i.e., they are generators (Section 5.3) of the unsteady topology.

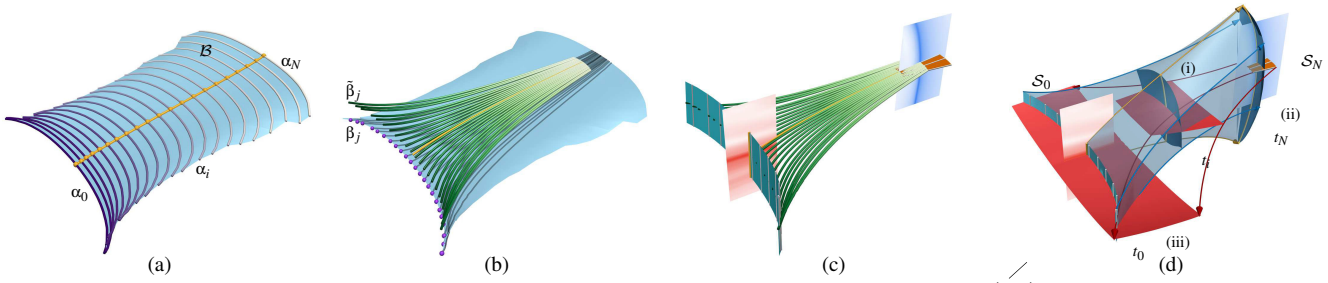

Figure 3: *Overview of our approach: (a) Bifurcation lines α_i (time purple to white) are extracted in $\mathbf{w}(\mathbf{x},t)$ at each time step and triangulated ($\mathcal{B}$) in space-time. (b) Streamlines of $\bar{\mathbf{u}}(\bar{\mathbf{x}})$ constrained to $\mathcal{B}$ (β_j, black, seeded at spheres) are refined toward hyperbolic trajectories ($\tilde{\beta}_j$, green to white) within the hyperbolic path surface. (c) The major ($\boldsymbol{\xi}_1$) and minor ($\boldsymbol{\xi}_3$) Lyapunov vectors at the end points of each hyperbolic trajectory are approximately perpendicular to the respective FTLE ridge, and used as seeding directions (white tubes, shown exaggerated), resulting in seeding manifolds $\mathcal{S}_0$ (cyan), $\mathcal{S}_N$ (orange). The medium Lyapunov vectors $\boldsymbol{\xi}_2$ are approximately tangential to the hyperbolic path surface. (d) Space-time streamvolumes (transparent blue, forward only) are seeded at $\mathcal{S}_0$, $\mathcal{S}_N$, whose time-slices are streak surfaces (opaque red and blue). A straightforward extension of the 2D method [HS20] would instead refine paths of saddle-type critical points ((a), yellow) toward hyperbolic trajectories ((b),(c), yellow). The resulting streak line ((d)(i), yellow) would miss most of the surface-type LCS ((d), blue).*

3.3. Streak-Based Topology

Instead of extracting ridges from the FTLE fields, LCS can also be obtained by seeding generalized streak manifolds along the hyperbolic path surfaces (Sections 1 and 2). For each HT contained in the HPS, a reverse-time streak 2-manifold is seeded on the segment $\mathbf{x}(t_N) \pm \delta \cdot \boldsymbol{\xi}_1(t_N)$ oriented along of the minor Lyapunov vector $\boldsymbol{\xi}_1$ (see Figure 3c) with segment length 2δ (discussed in Section 5.1), yielding the repelling LCS ((iii) in Figure 3d). Seeding a respective forward-time streak 2-manifold on the segment $\mathbf{x}(t_0) \pm \delta \cdot \boldsymbol{\xi}_3(t_0)$ in direction of the major Lyapunov vector $\boldsymbol{\xi}_3(t_0)$ yields the attracting LCS ((ii) in Figure 3d), correspondingly. Notice that each LCS is represented by the union of all respective 2-manifolds, resulting in a 3-manifold in space-time, whose isotemporal section represents the LCS at a given time. The resulting space-time seeding surfaces $\mathcal{S}_0, \mathcal{S}_N$ (Figure 3c) exhibit varying initial times t_0^k, t_N^k. A straightforward extension to 3D [BW09] would only consider a single, strongest DHT contained in the HPS (yellow in Figure 3).

Streak-based topology generalizes VFT to the time-dependent case, because streaklines are identical to streamlines in steady vector fields, and because the notion of a critical point in steady VFT, which corresponds to a streamline that degenerates to a single point, is replaced with that of a HPS, which can be considered a streak surface that degenerates to a streakline [SW10, USE13]. Since in the limit, as integration time approaches infinity, a subset of the ridges in the FTLE field of a steady vector field corresponds to the separatrices in steady VFT [FGRT17], the streak-based topology coincides with VFT for steady flows defined by saddle-type critical points and bifurcation lines (see Section 5.1).

4. Method

The time-dependent 3D vector field topology is extracted in three steps. We first locally extract candidate lines and surfaces in the 4D space-time domain (Section 4.1), which, in a second, global step, are refined toward HTs and HPSs (Section 4.2), and subsequently used for streak manifold generation (Section 4.3). Figure 3 provides an overview. In Section 4.4, we discuss the consistency with 3D VFT, and in Section 4.5 the overall properties of our approach. More details can be found in the supplemental material.

4.1. Candidate Surfaces and Lines

Taking an instantaneous view of hyperbolic path surfaces in the steady 4D space-time vector field $\bar{\mathbf{u}}(\bar{\mathbf{x}}) := (\mathbf{u}(\mathbf{x},t),1)^\top, \bar{\mathbf{x}} := (\mathbf{x},t)^\top$, they can be seen as bifurcation surfaces [HS19], i.e., locations where the space-time Jacobian $\nabla\bar{\mathbf{u}}(\bar{\mathbf{x}})$ has only real eigenvalues, and $\bar{\mathbf{u}}(\bar{\mathbf{x}})$ lies in the plane spanned by its two eigenvectors $\bar{\boldsymbol{\eta}}_2(\bar{\mathbf{x}}), \bar{\boldsymbol{\eta}}_3(\bar{\mathbf{x}})$, that belong to its two medium eigenvalues $\mu_2(\bar{\mathbf{x}}) \leq \mu_3(\bar{\mathbf{x}})$. This is a direct extension of the concept of swirling particle cores [WSTH07], which employs the reduced velocity criterion [SH95]. Similarly, since the space-time Jacobian has exactly one zero eigenvalue, whose eigenvector is the feature flow field $\mathbf{f} = -\nabla\mathbf{u}^{-1}\mathbf{u}_t$, this definition is reduced to moving 3D bifurcation lines in the Galilean-invariant frame of reference $\mathbf{w}(\mathbf{x},t) = \mathbf{u}(\mathbf{x},t) - \mathbf{f}(\mathbf{x},t)$. In order to avoid inversion of the matrix $\nabla\mathbf{u}$, we instead solve the linear least squares problem

$$\int_{\mathbf{x}\in\mathcal{U}} \|\nabla\mathbf{u}(\mathbf{x},t)\mathbf{f}(\mathbf{x},t) + \mathbf{u}_t(\mathbf{x},t)\|^2 \rightarrow \min \tag{6}$$

for the unknown $\mathbf{f}(\mathbf{x},t)$ at each time step over a local neighborhood $\mathcal{U}$ of 10 grid nodes, with $\mathbf{u}_t(\mathbf{x},t) := \partial\mathbf{u}(\mathbf{x},t)/\partial t$, using the method by Günther and Theisel [GT20]. Generally, any reference frame, that minimizes a time derivative [GT20, RG20], could be employed. However, in our experiments, we were unable to achieve more consistent results than using a Galilean-invariant frame of reference. This has, however, no impact on the Galilean invariance or objectivity of the obtained topology (see Section 4.5).

Since two neighboring time steps $\mathbf{w}(\mathbf{x},t_1)$, $\mathbf{w}(\mathbf{x},t_2)$ belong to different observers, we found that using temporal derivatives of $\mathbf{w}(\mathbf{x},t)$ for constructing a feature flow field for parallel vectors lines [TSW*05], or temporal interpolation for tracking solutions in space-time grid cells [BP02] leads to unreliable and noisy results. Instead, we extract bifurcation lines in the 3D spatial domain by applying apply the parallel vectors operator to each time step, and

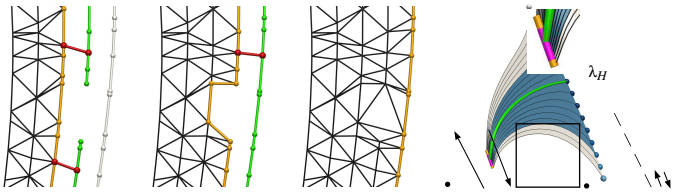

Figure 4: *(a)–(c) Three time steps in the space-time triangulation of parallel vectors lines. A front (orange) of polylines is triangulated with polylines in the candidate set (green), started from the nearest pairs of vertices (red). (d) Optimization of the seeding length δ. A space-time streak surface (white) is computed from an initially large offset (orange). At its end points, the FTLE values (spheres, white to blue) in relation to the FTLE λ_H of the HT are used to determine (along arrows) the seeding offset (magenta).*

filter the resulting lines by feature strength and length [MSE13]. The resulting sequence of polylines is triangulated in space-time using an approach based on the ball-pivoting algorithm [BMR*99] for surface reconstruction of 3D point clouds. Similarly to the original algorithm, we perform the triangulation by advancing a front of edges. In each iteration, we insert the polylines of the next time step into a set of candidates for triangulation. Edges in the front are greedily advanced to candidate edges if they are closer than a cell diagonal, creating new triangles. At the end of each iteration, the remaining candidates are added to the front, and edges, which belong to time steps older than two, are removed from the front. See Figure 4 for an illustration of the procedure.

Subsequently, we extract the paths of saddle-type critical points in $\mathbf{w}(\mathbf{x},t)$. Those paths that are not contained in the obtained triangulation are added to the set of candidate manifolds. These additional paths address isotropic saddle-type (Figure 2a) and spiral saddle-type critical points (Figures 5a and 5e).

4.2. Refinement

The candidate surfaces from Section 4.1 are first decomposed into an ordered set of candidate lines. For this, we integrate the space-time vector field $\bar{\mathbf{u}}(\bar{\mathbf{x}})$ projected onto the surface. The projected 4D vector field is converted into a piecewise constant vector field on each triangle. We then seed a streamline at the center of each edge on the boundary of the candidate surface, and integrate it according to Tricoche at al. [TGS06]. If the projected velocity points outside of the triangle at the boundary edge, we use backward-time integration. By construction of the space-time surface, streamline integration always starts and ends on the surface boundary. This allows us to order the resulting candidate lines. Figure 3b shows an example.

We then refine each of the candidate lines using the method for finding distinguished hyperbolic trajectories due to Branicki and Wiggins [BW09], employing the modifications for increased stability for 2D flows [HS20], which extend to 3D straightforwardly. This amounts to transforming the localized flow along the candidate line into separated coordinates (Equation 4), where attracting and repelling directions can be integrated in opposing directions using a fixed-point iteration. We refer to Section 1.2 in the supplemental material for details. This computation also provides the Lyapunov vectors along each of the obtained pathlines.

4.3. Streak Manifold Generation

Let us now look at the algorithmic aspects of streak manifold seeding (Section 3.3). To generate a streak manifold from a single hyperbolic trajectory $\mathbf{x}(t)$ (isotropic case from Figure 2a), with corresponding Lyapunov exponents λ_i and Lyapunov vectors $\boldsymbol{\xi}_i(t)$, its attracting and repelling streak manifolds would be seeded at the end time t_N and starting time t_0, respectively, with a user-defined segment length δ^-, δ^+. For brevity, we only discuss seeding of the repelling manifold at time t_0. The attracting manifold is obtained by reversing the role of time. If the repelling manifold is one-dimensional, i.e., $\lambda_2 < 0 < \lambda_3$, we would seed a time line along the line segment $\mathbf{x}(t_0) \pm \delta^{\pm} \cdot \boldsymbol{\xi}_3(t_0)$ at time t_0 (Figure 3c). For a two-dimensional manifold, where $\lambda_1 < 0 < \lambda_2 \leq \lambda_3$, we would seed a time surface from the elliptic disc $\mathbf{x}(t_0) + \delta \sin(\alpha)\boldsymbol{\xi}_3(t_0) + \delta\cos(\alpha)\boldsymbol{\xi}_2(t_0)$ for $\alpha \in [-\pi, \pi]$ at time t_0, with user-defined length δ.

In practice, we need to generate a streak manifold from a hyperbolic path surface instead, with the HPS given (Section 4.2) as a sorted set of hyperbolic trajectories $\{\mathbf{x}^j(t)\}$, where each can be considered to possess a seeding structure as described above. Furthermore, all Lyapunov exponents λ_i^j are of equal sign for fixed i, and the HPS is tangential to the medium Lyapunov vectors $\boldsymbol{\xi}_2^j(t)$. For seeding the repelling manifold, we construct a space-time triangle mesh by triangulating the family of line segments $\mathbf{x}^j(t_0^j) + \delta^{\pm} \cdot \boldsymbol{\xi}_3^j(t_0^j)$. Note, that the initial times t_0^j are in general not constant. Analogously, also a 2-manifold seeding structure in space-time is obtained for the attracting manifold (see Figure 3c).

4.3.1. Streak Integration

We compute the time lines, seeded from the seeding segments, as streamsurfaces [Hul92] in the space-time vector field, which adds time as a fourth component to the vertex coordinates. From this streamsurfaces, a streakline at time t is obtained as the contour at isovalue t of the time component stored on the surface mesh.

The streak surfaces ("time surfaces") could be computed similarly to stream volumes in the space-time vector field, where isosurfaces of the time scalar would yield the streak surfaces. However, we found, that this leads to prohibitively large four-dimensional tetrahedral meshes for long integration times in turbulent flows. Therefore, the streak surfaces are computed using a minor modification of the time surface algorithm by Krishnan et al. [KGJ09]. Starting from the smallest time value in the space-time seeding mesh, we iteratively step forward in time. At each time step t, those vertices in the space-time mesh, that have a time value below t, are advected toward the current time step t, using a dynamically sized integration step. The remaining parts of the algorithm are performed as described in the original work, which results in a set of pathlines and a representation of the streak surface across the entire integration time. The resulting streak surfaces at time t, which contain vertices at times greater or equal to t, are clipped by time.

4.3.2. Determination of Seeding Lengths

Typically, the lengths δ^-, δ^+, and δ are user-defined and depend on the dataset as well as the available time interval for integration.

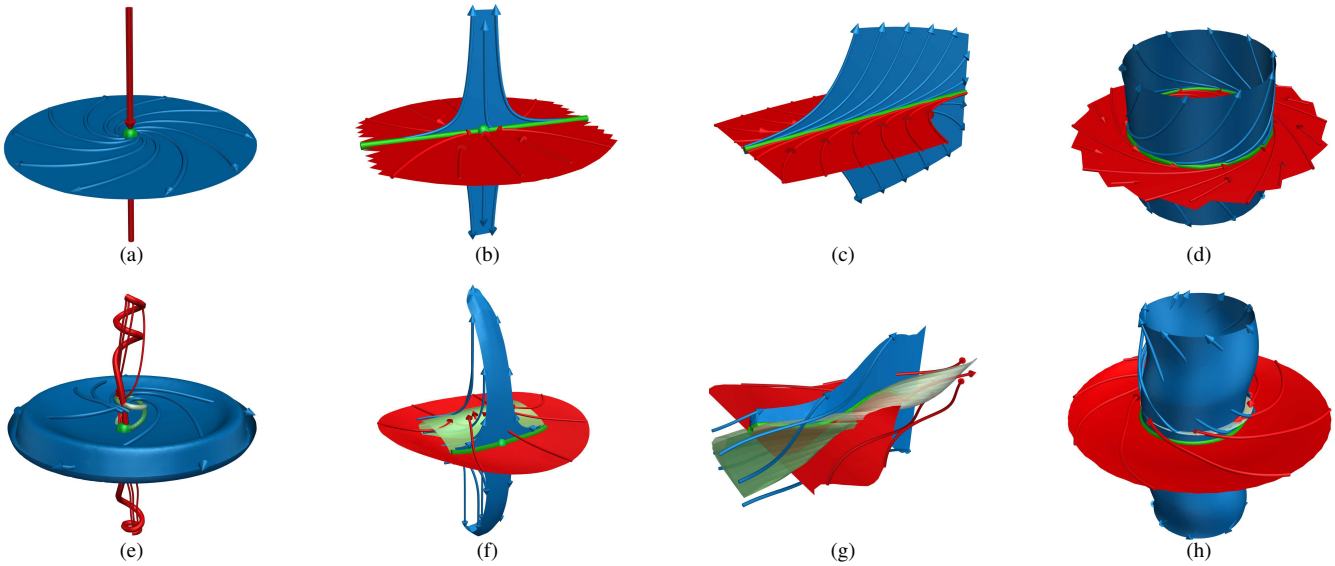

Figure 5: *Steady topological structures (top row), and their unsteady counterparts (bottom row). Spiral saddle-type critical point (a)(e), non-spiral saddle-type critical point on a bifurcation line (b)(f), bifurcation line without critical point (c)(g), and closed bifurcation line (d)(h) representing a saddle-type periodic orbit. Green: hyperbolic trajectories and hyperbolic path surfaces, blue/red: attracting/repelling LCS.*

Branicki and Wiggins [BW10, Appendix B] have shown, that for sufficiently small choices, the resulting manifolds are guaranteed to be contained within the respective finite-time invariant manifolds, and that the influence of this choice diminishes with increasing advection time. However, numerical datasets typically have limited time domains, making it important to select a length that is as large as possible, to ensure that the streak manifolds grow large enough in the available space-time domain of the dataset and the lifetime of the HT/HPS. We determine such a length using the following approach (see Figure 4d). From a user-defined maximum length $\delta_{\max}$, we compute the resulting streakline as a space-time streamsurface over the time interval of the hyperbolic trajectory, where we obtain the set of pathlines that are involved in its computation. If a new seed is inserted during the adaptive extraction [Hul92], we linearly interpolate the two involved pathline seeds, instead of the triangle edge, to obtain pathlines over the entire time interval. This results in a mapping between points on the regularly sampled streakline and its initial points on the seeding segment. Finally, starting from the hyperbolic trajectory, we determine the closest seeding point, such that the reverse-time localized FTLE [KPH*09] of the corresponding point on the streakline falls below a percentage of 50% of the FTLE λ_H at the HT, for which we obtained good results in our experiments. This approach is demonstrated in Figures 11g–11i.

4.4. Consistency with Steady Vector Field Topology

VFT of steady vector fields is known to coincide with the topology indicated by ridges in the FTLE fields, in the limit as advection time tends to infinity [FGRT17]. We further note, that for steady vector fields, the medium Lyapunov exponent λ_2 is zero, since the medium Lyapunov vector $\boldsymbol{\xi}_2$ describes perturbation in direction of the flow $\boldsymbol{\xi}_2(t) = \mathbf{u}(\mathbf{x}(t),t)$, and therefore HPSs degenerate to points or lines. We thus verify in the following, that the structures extracted from a steady vector field $\mathbf{u}(\mathbf{x},t) = \mathbf{u}_s(\mathbf{x})$ by our approach coincide with saddle-type critical points and bifurcation lines, and their invariant manifolds in the steady vector field $\mathbf{u}_s(\mathbf{x})$.

A steady vector field has zero time-derivative $\mathbf{u}_t(\mathbf{x},t) = \mathbf{0}$, and thus any reference frame, which minimizes a time derivative, coincides with the vector field itself, i.e., $\mathbf{w}(\mathbf{x},t) = \mathbf{u}_s(\mathbf{x})$ and $\mathbf{f}(\mathbf{x},t) = \mathbf{0}$. Saddle-type critical points, which do not lie on bifurcation lines, are thus extracted as temporal candidate lines ($\mathbf{x}(t) = \text{const}$), and the subsequent refinement does not change their location, since they are already hyperbolic trajectories. Candidate surfaces consist of temporal copies of the bifurcation lines in $\mathbf{u}_s(\mathbf{x})$. These are decomposed into surface streamlines (Section 4.2), which again represent copies of the bifurcation lines in $\mathbf{u}_s(\mathbf{x})$ with an additional time-parametrization. Refinement of these candidate lines toward hyperbolic trajectories is equivalent to refining the steady bifurcation lines toward streamlines. This process is similar to the technique of Machado et al. [MSE13, MBES16], who use the same algorithm for extraction of 3D bifurcation lines and 2D hyperbolic trajectories in space-time. And thus, our seeding manifolds coincide with the usual seeding approaches for saddle-type critical points and bifurcation lines in traditional VFT. Our concept is consistent with VFT, since streak surfaces and streamsurfaces are identical for steady vector fields. Non-hyperbolic features from steady VFT, such as source- or sink-type critical points and periodic orbits as well as invariant tori, do not have to be considered, as discussed next.

4.5. Properties of our Unsteady Vector Field Topology

We now discuss the desirable properties for unsteady topology, as proposed by Bujack et al. [BYH*20]. Our method is consistent with the subset of steady vector field topology (Section 4.4) defined by saddle-type critical points and bifurcation lines. As we only consider hyperbolic structures, consistent with LCS, the missed fea-

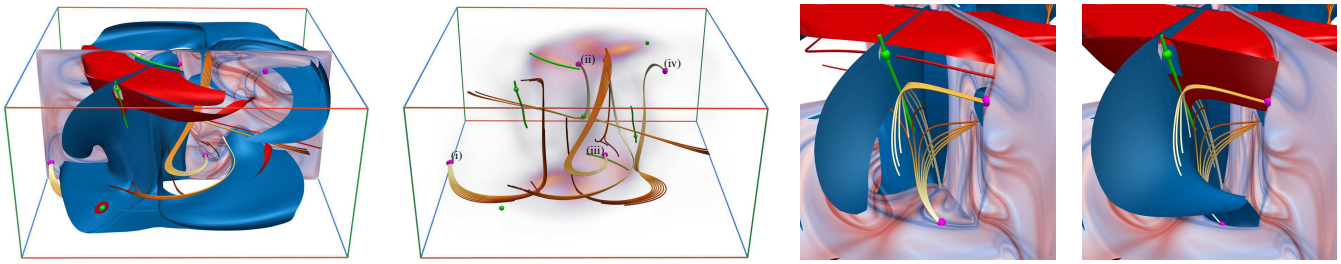

(a) (b) (c) (d)

Figure 6: *Steady 3D vector field topology of a single time step in the Convective Flow (saddle-type critical points and bifurcation lines green, invariant manifolds red and blue). Rakes (i–iv in (a),(b): seeds magenta, streamlines with integration time orange to white) show, that shear-induced ridges in the FTLE fields (section) are not included in the steady VFT. Seeding invariant manifolds of a saddle-type critical point (c) instead of its bifurcation line (d) misses parts of the FTLE ridges at same integration times (box). Enlarged region, see box in (a).*

tures in steady VFT are those, that do not contribute to hyperbolic separation. The spatial domain is only partially partitioned due to time-dependence, and since LCS and FTLE ridges need sufficient time to grow. This also implies, that Lagrangian invariance and a non-trivial spatial partition are generally mutually exclusive. Most non-trivial partitions are induced by intersections of the streak manifolds themselves, i.e., at the presence of unsteady saddle connectors (Section 5.3). Our topology is Lagrangian-invariant, as it is defined by pathlines and streak surfaces, and thus also Galilean-invariant and objective. Note, that even the extraction using initial candidates in a possibly not even Galilean-invariant frame of reference would yield objective topological features in our approach, albeit some initial candidates could possibly be missed. We refer to Branicki and Wiggins [BW10, Sec. 2] for an in-depth discussion.

5. Results

In the following, we first discuss properties of 3D steady vector field topology in relation to the FTLE and our 3D time-dependent topology at specific synthetic examples. We then evaluate the performance and accuracy, and apply our approach to numerical datasets. Our prototype is implemented in C++, with OpenMP for parallelization. All computations were performed on a desktop computer with 64 GB of RAM and an Intel i7-7700K CPU. We note, that large parts of the algorithm, such as the parallel vectors extraction, could be further parallelized on the GPU. For comparison with the work of Rojo and Günther [RG20], we extended their 2D prototype to 3D, and used a neighborhood of 41^3 nodes. Ridge surfaces were extracted using the prototype provided by Schultz et al. [STS09]. We refer to the accompanying video for animations of the figures. Additional analysis of the stability of our method can be found in the supplemental material.

5.1. FTLE and Separation in Steady Vector Fields

Instantaneous Convective Flow. We consider the instantaneous topology of a single time step of the Convective Flow dataset (Section 5.8), and compare it with FTLE ridges (Figure 6a–6d). For this, we integrate the invariant manifolds of the VFT using the same integration time as the FTLE. In this dataset, the FTLE exhibits many more ridges than captured by the separatrices (Figure 6a). Investigating their separating behavior by seeding rakes across these ridges (Figure 6b), we find, that ridges not captured by VFT are shear-induced. We conclude, that employing the FTLE for flow analysis requires careful examination of the separating behavior of each ridge. The dataset further contains saddle-type critical points, which lie on bifurcation lines. Comparing the corresponding invariant manifolds, that can be either seeded from the critical point (Figure 6c) or the bifurcation line (Figure 6d), we find that seeding from the bifurcation line results in topological structures more consistent with the FTLE. For this reason, our unsteady approach favors bifurcation lines over critical points, i.e., we omit critical points lying on bifurcation lines (e.g., Figure 11c).

Bounded ABC Flow. The ABC flow with standard parameters $A=\sqrt{3}, B=\sqrt{2}, C=1$ is an analytical solution of Euler's equation, which is commonly used as a benchmark for Lagrangian analysis [Hal01]. Generally, periodic spatial boundaries with fundamental domain $[0,2\pi]^3$ are assumed. However, when taking this steady vector field as bounded, as is common for numerical datasets, it exhibits no VFT structures, i.e., no critical points, nor periodic orbits or invariant tori. The FTLE, on the other hand, exhibits ridges, which separate the domain into regions of similar flow behavior. Separatrices of bifurcation lines also extract these structures (Figure 8a), which motivates their inclusion in VFT and thus in our time-dependent topology.

5.2. Kinematic Test Cases

We construct a set of simple test cases by translating a steady vector field along a curve, i.e., the unsteadiness is of kinematic rather than dynamic nature. Such synthetic examples are commonly used as benchmark for unsteady topology [BW09, SW10, USE13]. Note, that this translation does not correspond to a reference frame transformation of the steady vector field. Starting from steady configurations of topological structures, we construct their unsteady counterparts, as captured by our unsteady topology, by translation along a Lissajous curve [USE13]. Figure 5 shows the constructed cases, which provide the building blocks for 3D unsteady vector field topology. Instantaneous saddle-type critical points, which do not lie on a bifurcation line, are typically found in regions, where the Jacobian exhibits complex eigenvalues, since in that case two of their real parts are equal in a numerically stable way (Figure 5a and

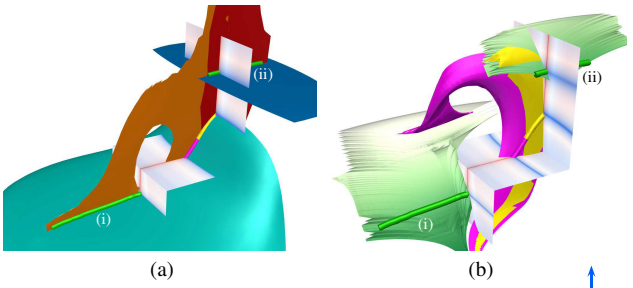

Figure 7: *Saddle connectors: heteroclinic (yellow) and homoclinic (magenta) orbits between two hyperbolic path surfaces ((i),(ii), green), in a single time step (a) and time projection (b) including the connectors from (a). The repelling (orange/red) and attracting (cyan/blue) manifolds intersect along surfaces in 4D space-time. Ridges in the forward- and backward-time FTLE fields intersect both along hyperbolic path surfaces and along saddle connectors.*

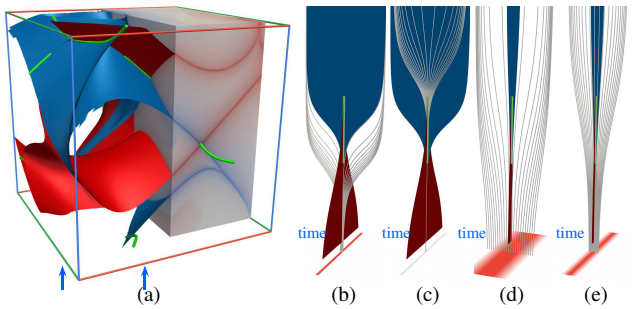

Figure 8: *(a) ABC Flow: while traditional VFT is empty, bifurcation lines (green) and their invariant manifolds (red/blue) capture the separating behavior of the flow consistently with the FTLE. (b)–(e) Scale-dependency of the FTLE (red, bottom). Strongly separating LCS (b) appears weak at smaller scales (c). Weakly separating LCS (d) appears strong at larger scales (e). Hyperbolic trajectory (green) and attracting/repelling streak manifolds (blue/red).*

5e; see also Figure 2). Bifurcation lines can either be open (Figure 5c and 5g) or closed (Figure 5d and 5h), and they may contain a saddle-type critical point (Figure 5b and 5f). As discussed in the previous section, we favor bifurcation lines over critical points if both are present. Note, that bifurcation lines do not extract general saddle-type periodic orbits, but only those that entirely represent bifurcation lines [MSE13]. Those parts of the hyperbolic path surface, on which pathlines have enough time to recirculate, coincide with recirculation surfaces [WRT18].

5.3. Saddle Connectors

Intersections of streak manifolds play an important role in unsteady flow analysis [MW98], and they manifest themselves as false-positive HTs (FTLE ridge intersections). Analogously to 2D unsteady flows [HS20], where such connectors can be related to saddle connectors in the corresponding steady 3D space-time vector field [TWHS03], the corresponding configurations in 3D unsteady flow can be found in the steady 4D space-time vector field [HRS18]. As indicated by the authors, two 4D saddle-type critical points can posses surfaces of saddle connectors. To demonstrate, that 3D unsteady flow can also exhibit such configurations, we extend the synthetic 2D example [HS20, Figure 6] to 3D. Figure 7 shows the resulting hyperbolic path surfaces as well as their homoclinic and heterclinic connection surfaces, which we extracted geometrically by intersecting the resulting streak manifolds. Our approach does not extract these (false-positive) saddle connectors, as opposed to FTLE-based approaches [USE13].

5.4. Scale-Dependency of the FTLE

The separation, that induces an FTLE ridge, is defined by its curvature [SLM05]. This makes analysis using FTLE ridges even more challenging, since the curvature depends on the spatial scale/resolution of the FTLE field. The choice of resolution implies a choice of scale, as we demonstrate at two simple 2D examples in Figure 8. These examples contain a small hyperbolic region, where we extract a hyperbolic trajectory, of varying strength (large in Figures 8b and 8c, small in Figures 8d and 8e). In both cases, the corresponding FTLE ridge can be extracted with high or low curvature,

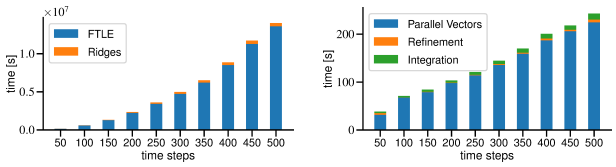

Figure 9: *Performance analysis. Forward- and backward-time FTLE ridge extraction at each time step (a), and our method over the entire dataset (b). Notice the time scale difference of about 10^5.*

depending on FTLE resolution. Our locally extracted topology, on the other hand, has no such scale parameter. Instead, the resulting streak manifolds exhibit different levels of growth. In practice (see also Section 5.8), hyperbolic trajectories can be filtered by strength in order to obtain only the most relevant topological structures.

5.5. Performance

We compare the computational costs of our approach with the direct extraction of LCS from FTLE fields (Figure 9) at the synthetic unsteady saddle dataset (Section 5.2). The direct approach requires the computation of a dense set of pathlines. For comparison, we keep a rather low fixed resolution of 300^3 samples and extract ridge surfaces in the forward and backward FTLE fields for a varying number of time steps (Figure 9a). The computational costs depend linearly on both the number of samples and number of integration steps, however the extraction needs to be repeated at each time step, leading to an asymptotically quadratic complexity with respect to the number of time steps. In practice, one would need to increase the resolution of the FTLE fields with increasing advection times in order to accurately resolve the stretching and folding of the LCS, which would result in exponential computational complexity. Our method, on the other hand, has no resolution parameter, but only extracts parallel vectors lines from each original grid cell, which is resolved at 41^3 nodes. Its computational costs also depend linearly on the number of nodes, and thus on the number of time steps (Figure 9b). Since the refinement and streak integration is performed

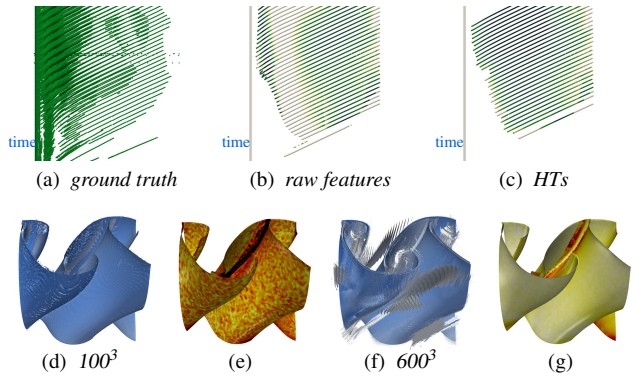

(a) *ground truth* (b) *raw features* (c) *HTs*

(d) 100^3 (e) (f) 600^3 (g)

Figure 10: *Convergence of FTLE ridges to streak topology. The distance of parallel vectors lines (b) to FTLE ridge intersections (a) is decreased by refinement toward hyperbolic trajectories (c). Distance in dark green (zero) to white (one cell diagonal). The temporal evolution (time evolves upward) of sections with the plane z=5 is shown (Figure 11). For increasing resolutions of FTLE, ridges (d)(f) converge toward streak manifolds (e)(g). Distance to FTLE ridge shown in color from white to black (one cell diagonal).*

over the entire time span of the dataset, this computation yields the LCS for all times. We thus conclude, that our method is typically several orders of magnitude faster than a direct extraction, and additionally no numerically challenging evaluation of the flow map or ridge extraction is necessary.

5.6. Accuracy

We compare the hyperbolic trajectories and streak manifolds obtained using our method with ridges in the FTLE fields, at the example of the von Kármán Vortex Street dataset (discussed in detail in Section 5.7). On the plane $z = 5$, we compute the forward and backward FTLE fields with resolution 2000×1000 at each time step of the dataset. We extract local maxima in the product of the two FTLE fields, where we simplify the scalar topology by filtering critical point pairs with persistence below 2% of the maximum, using the implementation in the Topology Toolkit [TFL*17]. Due to numerical aliasing, we obtain false-positives near the obstacle (Figure 10a), but otherwise a reasonable, computationally feasible approximation of the FTLE ridge intersections. From these, we obtain the distance of the sections of the parallel vectors lines as well as the refined hyperbolic trajectories (Figure 10b and 10c). We find, that the raw solutions are refined well toward FTLE ridge intersections. Note, that the lines in Figure 10a–10c depict the evolution of sections rather than pathlines. Finally, we compare distances of part (Figure 11f, box) of the attracting streak manifold to the corresponding FTLE ridge surfaces (Figure 10d–10g). The distance decreases with FTLE resolution and thus accuracy increases. The same ridge filter parameters were used for all resolutions, which makes numerical aliasing in the FTLE computation visible.

5.7. Von Kármán Vortex Street

The CFD flow of a von Kármán vortex street forming behind a cuboid obstacle was computed on a domain with extent $[0,60] \times [0,10]$ m^3 on a $61 \times 41 \times 61$ uniform grid. The dataset contains 801 time steps on the time interval $[0,0.8]$ s. The inflow velocity varies linearly from 200 m s^{-1} to 250 m s^{-1} with distance from the base wall. Since our dataset exhibits large amounts of numerical noise, we computed derivatives using convolution with derivatives of Gaussians, with standard deviations $\sigma_s = 0.4$ m for spatial derivatives, and $\sigma_t = 0.002$ s for time derivatives. Computation across the entire dataset took 6546 s in total (derivatives and frame of reference: 3197 s, parallel vectors: 2261 s, refinement: 276 s, streak integration: 812 s). The raw features and resulting hyperbolic trajectories are shown in the accompanying video. Extraction of the ridges in Figure 10f, on the other hand, took 253 s, and the corresponding flow map took 2800 s, which only yields a small part of the attracting LCS in a single time step.

In previous work, Branicki and Wiggins [BW09] propose to use critical points in the lab frame of reference as candidates for refinement toward HTs. For comparison, we compute the time-dependent topology from critical points in our Galilean-invariant frame of reference (Figure 11c). This only captures small parts of those LCS, where the corresponding bifurcation lines contain a saddle-type critical point. Rojo and Günther [RG20] propose to extract steady VFT in their optimal frame of reference, which results in structures, that are not well aligned with LCS (Figures 11d and 11e), and exhibit additional deviations in vertical direction. Furthermore, the computationally more demanding optimal reference frame does not yield better initial candidates than the Galilean-invariant frame of reference. We also found, that integration along observer motion $\mathbf{f}(\mathbf{x},t)$ of both frames of reference is unstable near the obstacle (Figures 11a and 11b), and we were thus unable to recover missing features using the method proposed by Hofmann and Sadlo [HS20].

5.8. Convective Flow

This dataset has extent $[0,10] \times [0,5] \times [0,10]$ m^3 on a $61 \times 31 \times 61$ uniform grid. It contains a CFD simulation of bouyant air flow in a closed container with no-slip boundaries. To ease discussion of this turbulent flow, we select 200 time steps over the time interval $[4,9]$ s. Computation took 810 s in total (derivatives and frame of reference: 375 s, parallel vectors: 177 s, refinement: <1 s, streak integration: 257 s). The FTLE computed from this dataset exhibits a large amount of thinly folded ridges. However, we found, that most of them correspond to weak separation and shear flow (see also Sections 5.1 and 5.4). Figure 12 shows pathline rakes for some of these cases. This makes flow analysis using the FTLE infeasible, since it is unclear how to filter false-positive ridges. In the Galilean-invariant frame of reference, the dataset contains only short lived bifurcation lines, which our method is unable to accurately refine. The separating structure is largely generated by strongly hyperbolic spiral saddle critical points at the domain center, which our approach captures. It also extracts the many weakly hyperbolic saddle-type critical points, which possess streak manifolds of limited growth (I–III in Figure 12a), and which could be filtered by a hyperbolicity threshold.

5.9. Discussion and Limitations

Our method has two major limitations. First, it depends on extracting bifurcation lines in a suitable frame of reference using the par-

allel vectors operator. This extraction can exhibit false negatives, especially for feature lines with high curvature [MSE13]. Finding an optimal frame of reference is also challenging in the presence of turbulence (see Section 2.2 in the supplemental material). A good frame of reference for these cases has yet to be found and would be required for ensuring a robust extraction of the topology. Furthermore, the refinement of candidates toward hyperbolic trajectories depends on the temporal length of the candidate lines. This is not only limited by the time domain of the dataset, but also on the lifetime interval of the raw feature line. The available integration time may also be further shortened if domain boundaries are reached. The accuracy of the refinement can be assessed by computing the FTLE in the vicinity and time interval of the feature line. If no sharp ridges are present, no accurate refinement can be guaranteed.

6. Conclusion

We presented an approach to local extraction of vector field topolgy in 3D time-dependent vector fields, which extends previous streakline-based approaches [MSE13, HS20] from 2D to 3D. We have identified the necessity of including spatial bifurcation lines, we have shown that our topology is aligned with LCS defined by the FTLE, and that for steady flows, our approach coincides with a subset of traditional steady vector field topology. Unlike FTLE-based approaches, we obtain an explicit geometric LCS representation, and our approach does not suffer from false-positive FTLE ridges (intersections). We demonstrated that our geometric representation lends itself to further flow analysis, and that our approach is typically orders of magnitude faster and more accurate than FTLE-based approaches. As future work, we would like to further investigate unsteady topology induced by shear, and unsteady equivalents to invariant tori, i.e., elliptic structures.

Acknowledgments

This work was supported by the Deutsche Forschungsgemeinschaft (DFG, German Research Foundation) under the SFB / TRR 191 "Symplectic Structures in Geometry, Algebra and Dynamics", and under Germany's Excellence Strategy EXC 2181/1 - 390900948 (the Heidelberg STRUCTURES Excellence Cluster). Open access funding enabled and organized by Projekt DEAL. [Correction added on 05 November 2021, after first online publication: Projekt Deal funding statement has been added.]

References

[BMR*99] BERNARDINI F., MITTLEMAN J., RUSHMEIER H., SILVA C., TAUBIN G.: The ball-pivoting algorithm for surface reconstruction. *IEEE transactions on visualization and computer graphics 5*, 4 (1999), 349–359. 5

[BP02] BAUER D., PEIKERT R.: Vortex tracking in scale-space. In *Proc. Symposium on Data Visualisation* (2002), pp. 233–ff. 4

[BSDW12] BACHTHALER S., SADLO F., DACHSBACHER C., WEISKOPF D.: Space-time visualization of dynamics in Lagrangian coherent structures of time-dependent 2D vector fields. In *Proc. of International Conference on Information Visualization Theory and Applications* (2012), pp. 573–583. 2

[BW09] BRANICKI M., WIGGINS S.: An adaptive method for computing invariant manifolds in non-autonomous, three-dimensional dynamical systems. *Physica D: Nonlinear Phenomena 238*, 16 (2009), 1625–1657. 2, 3, 4, 5, 7, 9, 12

[BW10] BRANICKI M., WIGGINS S.: Finite-time Lagrangian transport analysis: stable and unstable manifolds of hyperbolic trajectories and finite-time Lyapunov exponents. *Nonlinear Processes in Geophysics 17*, 1 (2010), 1–36. 6, 7

[BYH*20] BUJACK R., YAN L., HOTZ I., GARTH C., WANG B.: State of the art in time-dependent flow topology: Interpreting physical meaningfulness through mathematical properties. *Computer Graphics Forum 39*, 3 (2020), 811–835. 2, 6

[EGM*94] EBERLY D., GARDNER R., MORSE B., PIZER S., SCHARLACH C.: Ridges for image analysis. *Journal of Mathematical Imaging and Vision 4*, 4 (1994), 353–373. 3

[FGRT17] FRIEDERICI A., GÜNTHER T., RÖSSL C., THEISEL H.: Finite time steady vector field topology – theoretical foundation and 3D case. In *Proc. Vision, Modeling and Visualization* (2017). 4, 6

[GGT17] GÜNTHER T., GROSS M., THEISEL H.: Generic objective vortices for flow visualization. *ACM Transactions on Graphics 36*, 4 (2017), 141:1–141:11. 2

[GGTH07] GARTH C., GERHARDT F., TRICOCHE X., HAGEN H.: Efficient computation and visualization of coherent structures in fluid flow applications. *IEEE Transactions on Visualization and Computer Graphics 13*, 6 (2007), 1464–71. 2

[GT20] GÜNTHER T., THEISEL H.: Hyper-objective vortices. *IEEE Transactions on Visualization and Computer Graphics 26*, 3 (2020), 1532–1547. 2, 4

[Hal01] HALLER G.: Distinguished material surfaces and coherent structures in three-dimensional fluid flows. *Physica D: Nonlinear Phenomena 149*, 4 (2001), 248–277. 2, 3, 7

[HH91] HELMAN J. L., HESSELINK L.: Visualizing vector field topology in fluid flows. *IEEE Computer Graphics and Applications 11*, 3 (1991), 36–46. 1

[HMTR18] HADWIGER M., MLEJNEK M., THEUSSL T., RAUTEK P.: Time-dependent flow seen through approximate observer Killing fields. *IEEE Transactions on Visualization and Computer Graphics 25*, 1 (2018), 1257–1266. 2

[HRS18] HOFMANN L., RIECK B., SADLO F.: Visualization of 4D vector field topology. *Computer Graphics Forum 37*, 3 (2018), 301–313. 8

[HS19] HOFMANN L., SADLO F.: The dependent vectors operator. *Computer Graphics Forum 38*, 3 (2019), 261–272. 2, 4

[HS20] HOFMANN L., SADLO F.: Extraction of distinguished hyperbolic trajectories for 2D time-dependent vector field topology. *Computer Graphics Forum 39*, 3 (2020), 303–315. 2, 4, 5, 8, 9, 10, 12

[Hul92] HULTQUIST J. P.: Constructing stream surfaces in steady 3D vector fields. In *Proc. IEEE Conference on Visualization* (1992), pp. 171–178. 5, 6

[ISW02] IDE K., SMALL D., WIGGINS S.: Distinguished hyperbolic trajectories in time-dependent fluid flows: analytical and computational approach for velocity fields defined as data sets. *Nonlinear Processes in Geophysics 9* (2002), 237–263. 2, 3

[KGJ09] KRISHNAN H., GARTH C., JOY K.: Time and streak surfaces for flow visualization in large time-varying data sets. *IEEE Transactions on Visualization and Computer Graphics 15*, 6 (2009), 1267–1274. 3, 5

[KPH*09] KASTEN J., PETZ C., HOTZ I., NOACK B. R., HEGE H.-C.: Localized finite-time Lyapunov exponent for unsteady flow analysis. In *Proc. Vision, Modeling and Visualization* (2009), pp. 265–276. 6

[MBES16] MACHADO G. M., BOBLEST S., ERTL T., SADLO F.: Space-time bifurcation lines for extraction of 2D Lagrangian coherent structures. *Computer Graphics Forum 35*, 3 (2016), 91–100. 2, 6

[MSE13] MACHADO G. M., SADLO F., ERTL T.: Local extraction of bifurcation lines. In *Proc. Vision, Modeling and Visualization* (2013), pp. 17–24. 1, 4, 6, 8, 10

[MW98] MALHOTRA N., WIGGINS S.: Geometric structures, lobe dynamics, and Lagrangian transport in flows with aperiodic time-dependence, with applications to Rossby wave flow. *Journal of nonlinear science 8*, 4 (1998), 401–456. 8

[PC87] PERRY A. E., CHONG M. S.: A description of eddying motions and flow patterns using critical-point concepts. *Annual Review of Fluid Mechanics 19*, 1 (1987), 125–155. 1

[PR99] PEIKERT R., ROTH M.: The parallel vectors operator: A vector field visualization primitive. In *Proc. IEEE Visualization* (1999), pp. 263–270. 2

[RG20] ROJO I. B., GÜNTHER T.: Vector field topology of time-dependent flows in a steady reference frame. *IEEE Transactions on Visualization and Computer Graphics 26*, 1 (2020), 280–290. 2, 4, 7, 9, 12

[Rot00] ROTH M.: *Automatic Extraction of Vortex Core Lines and other Line-Type Features for Scientific Visualization*. PhD thesis, ETH Zurich, No. 13673, 2000. 1

[SH95] SUJUDI D., HAIMES R.: Identification of swirling flow in 3-D vector fields. In *Proc. 12th AIAA Computational Fluid Dynamics Conference* (1995). 4

[SJS20] SAGRISTÀ A., JORDAN S., SADLO F.: Visual analysis of the finite-time Lyapunov exponent. *Computer Graphics Forum 39*, 3 (2020), 331–342. 2

[SLM05] SHADDEN S. C., LEKIEN F., MARSDEN J. E.: Definition and properties of Lagrangian coherent structures from finite-time Lyapunov exponents in two-dimensional aperiodic flows. *Physica D: Nonlinear Phenomena 212*, 3-4 (2005), 271–304. 2, 8

[SP07] SADLO F., PEIKERT R.: Efficient visualization of Lagrangian coherent structures by filtered AMR ridge extraction. *IEEE Transactions on Visualization and Computer Graphics 13*, 6 (2007), 1456–1463. 2

[STS09] SCHULTZ T., THEISEL H., SEIDEL H.-P.: Crease surfaces: From theory to extraction and application to diffusion tensor MRI. *IEEE Transactions on Visualization and Computer Graphics 16*, 1 (2009), 109–119. 7

[SW10] SADLO F., WEISKOPF D.: Time-dependent 2-D vector field topology: An approach inspired by Lagrangian coherent structures. *Computer Graphics Forum 29*, 1 (2010), 88–100. 2, 4, 7

[TFL*17] TIERNY J., FAVELIER G., LEVINE J. A., GUEUNET C., MICHAUX M.: The topology toolkit. *IEEE Transactions on Visualization and Computer Graphics 24*, 1 (2017), 832–842. 9

[TGS06] TRICOCHE X., GARTH C., SCHEUERMANN G.: Fast and robust extraction of separation line features. In *Scientific Visualization: The Visual Extraction of Knowledge from Data*. Springer, 2006, pp. 249–263. 5

[TS03] THEISEL H., SEIDEL H.-P.: Feature flow fields. In *Proc. Symposium on Data Visualisation* (2003), pp. 141–148. 2

[TSW*05] THEISEL H., SAHNER J., WEINKAUF T., HEGE H.-C., SEIDEL H.-P.: Extraction of parallel vector surfaces in 3D time-dependent fields and application to vortex core line tracking. In *Proc. IEEE Visualization* (2005), pp. 631–638. 4

[TWHS03] THEISEL H., WEINKAUF T., HEGE H.-C., SEIDEL H.-P.: Saddle connectors – an approach to visualizing the topological skeleton of complex 3D vector fields. In *Proc. IEEE Visualization* (2003), pp. 225–232. 8

[USE13] ÜFFINGER M., SADLO F., ERTL T.: A time-dependent vector field topology based on streak surfaces. *IEEE Transactions on Visualization and Computer Graphics 19*, 3 (2013), 379–392. 2, 3, 4, 7, 8

[WRT18] WILDE T., RÖSSL C., THEISEL H.: Recirculation surfaces for flow visualization. *IEEE Transactions on Visualization and Computer Graphics 25*, 1 (2018), 946–955. 8

[WSTH07] WEINKAUF T., SAHNER J., THEISEL H., HEGE H.-C.: Cores of swirling particle motion in unsteady flows. *IEEE Transactions on Visualization and Computer Graphics 13*, 6 (2007), 1759–1766. 2, 4

[WTHS04] WEINKAUF T., THEISEL H., HEGE H.-C., SEIDEL H.-P.: Boundary switch connectors for topological visualization of complex 3D vector fields. In *Proc. Eurographics / IEEE VGTC Symposium on Visualization* (2004), pp. 183–192. 1

[WTS*07] WIEBEL A., TRICOCHE X., SCHNEIDER D., JAENICKE H., SCHEUERMANN G.: Generalized streak lines: Analysis and visualization of boundary induced vortices. *IEEE Transactions on Visualization and Computer Graphics 13*, 6 (2007), 1735–1742. 3

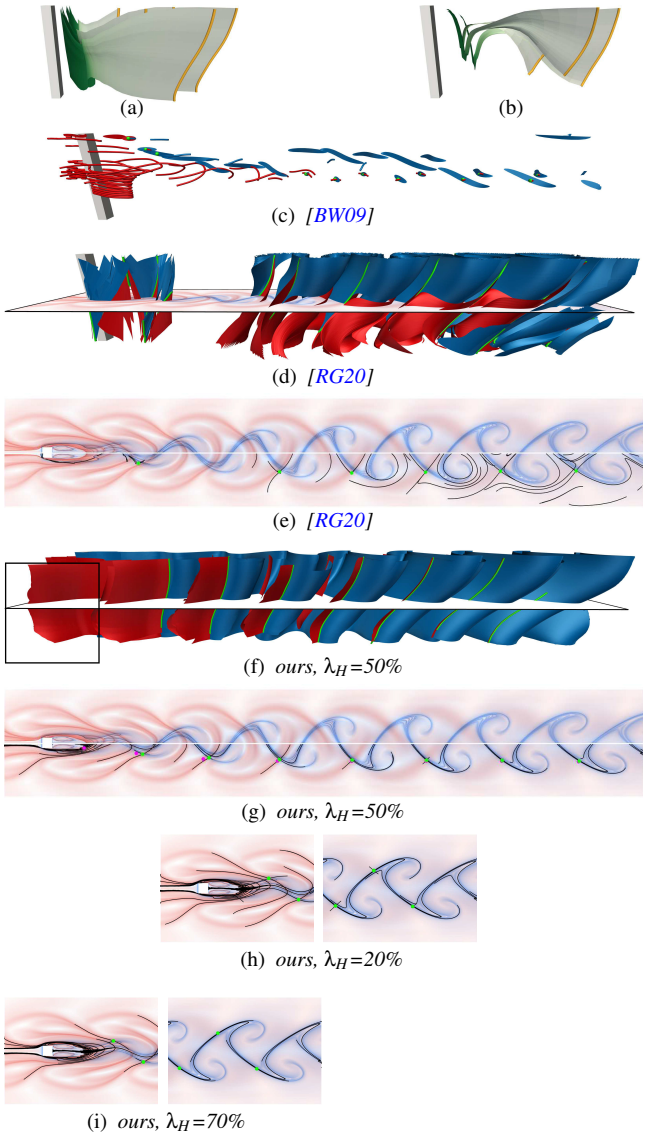

Figure 11: *Backward-time integration along observer motion* $\mathbf{f}(\mathbf{x},t)$ *for Galilean-invariant (a) and displacement-based (b) optimal frames of reference started on bifurcation lines in* $\mathbf{w}(\mathbf{x},t_0)$*. Considering saddle-type critical points in* $\mathbf{w}$ *as initial candidates for hyperbolic trajectories, i.e., a straightforward extension of the 2D method [HS20], misses most of the topological structure (c), while vector field topology in an optimal steady reference frame is not aligned with LCS (d),(e). Computed from a Galilean-invariant frame of reference, our method captures large parts of the topology, and is aligned with LCS (f),(g). Green: saddle points and bifurcation lines, blue/red: attracting/repelling LCS. Raw features shown in magenta in (g). (e) and (g) show cross-sections from (d) and (f), with manifolds slices shown in black. (g)–(i) Streak manifolds with seeding lengths (Section 4.3.2) from different percentages of FTLE.*

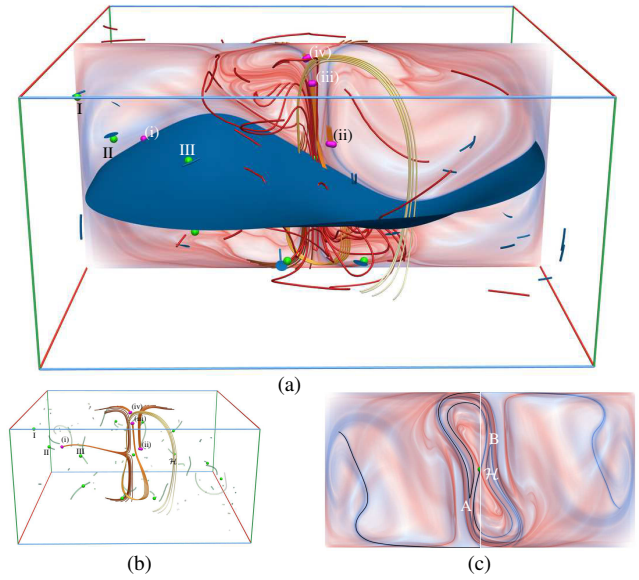

Figure 12: *Convective Flow dataset on time interval [4 s, 9 s]. (a) At t=5.5 s, the flow is governed by a strongly hyperbolic unsteady spiral saddle* $\mathcal{H}$*. Streak manifolds of weakly hyperbolic trajectories (I–III) exhibit limited growth. Most FTLE ridges are not captured by our topology because they are shear-induced or correspond to weak separation ((i)–(iv), pathline seeds magenta, pathlines in (b)). (c) Slice of the streak manifold (black) at t=6.5 s, for comparison. Notice point symmetry, where (A) corresponds to (B).*